



# Preliminary NBSR Design- Demonstration Element Thermal-Hydraulics and Structural Analyses

October 2022

Mauricio E. Tano  
Cole Mueller



*INL is a U.S. Department of Energy National Laboratory  
operated by Battelle Energy Alliance, LLC*

**DISCLAIMER**

This information was prepared as an account of work sponsored by an agency of the U.S. Government. Neither the U.S. Government nor any agency thereof, nor any of their employees, makes any warranty, expressed or implied, or assumes any legal liability or responsibility for the accuracy, completeness, or usefulness, of any information, apparatus, product, or process disclosed, or represents that its use would not infringe privately owned rights. References herein to any specific commercial product, process, or service by trade name, trade mark, manufacturer, or otherwise, does not necessarily constitute or imply its endorsement, recommendation, or favoring by the U.S. Government or any agency thereof. The views and opinions of authors expressed herein do not necessarily state or reflect those of the U.S. Government or any agency thereof.

**INL/RPT-22-69774  
Revision 0**

# **Preliminary NBSR Design-Demonstration Element Thermal-Hydraulics and Structural Analyses**

**Mauricio E. Tano  
SuJong Yoon**

**October 2022**

**Idaho National Laboratory  
Nuclear Science & Technology  
Idaho Falls, Idaho 83415**

**<http://www.inl.gov>**

**Prepared for the  
U.S. Department of Energy  
Office of Nuclear Energy  
Under DOE Idaho Operations Office  
Contract DE-AC07-05ID14517**

*Page intentionally left blank*

# CONTENTS

ACRONYMS.....	vi
1. Introduction.....	1
1.1 Objective.....	1
2. Problem Description.....	2
2.1 NBSR Geometry.....	2
2.2 Boundary Conditions.....	3
2.3 Material Properties.....	4
3. MoDELS.....	5
3.1 RELAP5-3D Thermal-Hydraulics model.....	6
3.2 Star-CCM+ CFD Model.....	8
3.3 Abaqus Mechanical Model.....	10
4. Study results.....	10
4.1 Thermal-Hydraulics Fields for Non-Isothermal Conditions.....	10
4.2 Oxide Growth Studies.....	16
4.3 Structural Analyses.....	17
5. Conclusions.....	17
6. REFERENCE.....	19

## FIGURES

Figure 1. NBSR DDE basket and fuel assembly. Top: Axial cut showing key dimensions. Bottom: Axial cut showing the end fittings of the fuel assembly and gap.....	2
Figure 2. NBSR DDE fuel assembly plates.....	3
Figure 3. Left: modeled internal geometry for the fluid flow in the NBSR test section. Right: Structure of the fuel plates in the NBSR fuel assembly.....	6
Figure 4. Nodal diagram for the RELAP5-3D NBSR model. ....	7
Figure 5. Domain geometry and mesh structure of NBSR DDE CFD model. ....	9
Figure 6. Grid Convergence behavior for various pressure drop across the DDE. ....	9
Figure 7. Pressure load and constraint boundary condition of ABAQUS model. ....	10
Figure 8. Left: total pressure drops predicted for all BOC configurations with the RELAP5-3D model. Right: pressure profiles predicted with the CFD model for all BOC configurations.....	11
Figure 9. CFD-calculated cross-sectional velocity distributions at various locations. Top: top set of plates. Bottom: bottom set of plates.....	12
Figure 10. Left: Maximum Channel Velocity as a function of Axial Position. Right: Average Channel Velocity as a function of Axial Position. ....	13
Figure 11. Top: Flow channels numbering. Bottom: mass flow rate per subchannel during BOC-6. ....	14
Figure 12. Comparison of the total temperature rise over the full section for all BOC configurations for the RELAP5-3D models; CFD results are equivalent within 0.1% of tolerance. ....	15
Figure 13. Left: Maximum fuel temperature as a function of the plate in the assembly for each irradiation Cycle. Right: Maximum temps predicted in the Fuel and Cladding by the CFD simulation. ....	15
Figure 14. Plate averaged heat transfer coefficients as a function of irradiation cycle. ....	16
Figure 15. Left: Average Oxide Thickness predicted on each plate throughout the irradiation campaign. Right: Maximum oxide Thickness predicted on each plate throughout the irradiation campaign.....	16
Figure 16. Left: ABAQUS calculation results for BOC6 (left: plate displacement, right: Von Mises stress). ....	17

## TABLES

Table 1. Power Density calculated and assumed in NBSR DDE fuel plates during the irradiation campaigns, the cycle time of each cycle was 31.5 days and the power during each irradiation campaign is assumed constant and equal to the Beginning of Cycle (BOC) power. ....	4
Table 2. Thermophysical properties for fuel and cladding materials. ....	5
Table 3. Maximum displacements and stresses for selected BOC configurations. ....	17

## ACRONYMS

AGR	Advanced Gas Reactor
ARIS	Advanced Reactors Information System
ARTIST	Advanced Reactor Technology Integral System Test
ASME	American Society of Mechanical Engineers
BANR	BWXT Advanced Nuclear Reactor
CBC	Closed Brayton cycle
DOD	Department of Defense
DOE	Department of Energy
FERC	Federal Energy Regulatory Commission
HALEU	High Assay Low-Enriched Uranium
HTGR	High-temperature gas reactor
IAEA	International Atomic Energy Agency
IHX	Intermediate Heat Exchanger
INL	Idaho National Laboratory
ITAAC	Inspections, Tests, Analyses, and Acceptance Criteria
MAGNET	Microreactor Agile Non-Nuclear Experimental Test
MMR	Micro Modular Reactor
MW	Mega Watts
NGTCC	Nuclear gas turbine combined cycle power plant concept
NIST	National Institute of Standards and Technology
NRC	Nuclear Regulatory Commission
PCHE	Printed circuit heat exchanger
SFR	Sodium fast reactor
SPM	Subcritical power modules
TRISO	tristructural isotropic
TRL	Technology Readiness Level
TRUST	Thermal-hydraulic Research Universal Scoping Tool
VHTR	Very-high temperature reactors

*Page intentionally left blank*

# **NBSR**

## **1. INTRODUCTION**

### **1.1 OBJECTIVE**

The United State High Performance Research Reactor (USHPRR) program aims to eliminate more than 200kg of High Enriched Uranium (HEU) from commerce annually by converting five U.S. high-performance research reactors and one associated critical assembly to Low Enriched Uranium (LEU) fuel using a high-density alloy of uranium-10 wt% molybdenum (U-10Mo). The National Bureau of Standards Reactor (NBSR) is one of five research reactors selected for this program. The objective of this report is to provide preliminary thermal-hydraulic and mechanical analyses of the hydrodynamic effects in the NBSR Design Demonstration Element (DDE) under conservative approximations for the plate power distribution. This report provides details on the modeling approach and the simulation results obtained, including pressure, flow velocity, temperature, and oxide layer over the design demonstration experiment for the irradiation cycles in the Belgian Reactor (BR)-2.

## 2. PROBLEM DESCRIPTION

The current section describes the geometry, boundary conditions, and material properties used for the analyses of the NBSR DDE.

### 2.1 NBSR GEOMETRY

The CAD-based geometry provided by SCK CEN and dimensions of NBSR DDE are depicted in Figure 1 and Figure 2. The NBSR DDE consists of a top coupling basket, bottom coupling basket, and the DDE basket which contains the fuel assembly. The NBSR consists of 34 fuel plates, 17 in the upper set and 17 in the lower set with 18 supporting cooling channels. These 17 plates are swaged into grooves in the side plates. In the figure the purple are unfueled aluminum plates that extend the length of the assembly. The grey are fuel plates. Each fuel plate consists of a 295.275 mm (11.625 in) fueled region length with additional clad extending on the top (1 in) and bottom (0.375 in) of each plate. The shorter span of clad is towards the midplane of the core to limit parasitic absorption of neutrons.

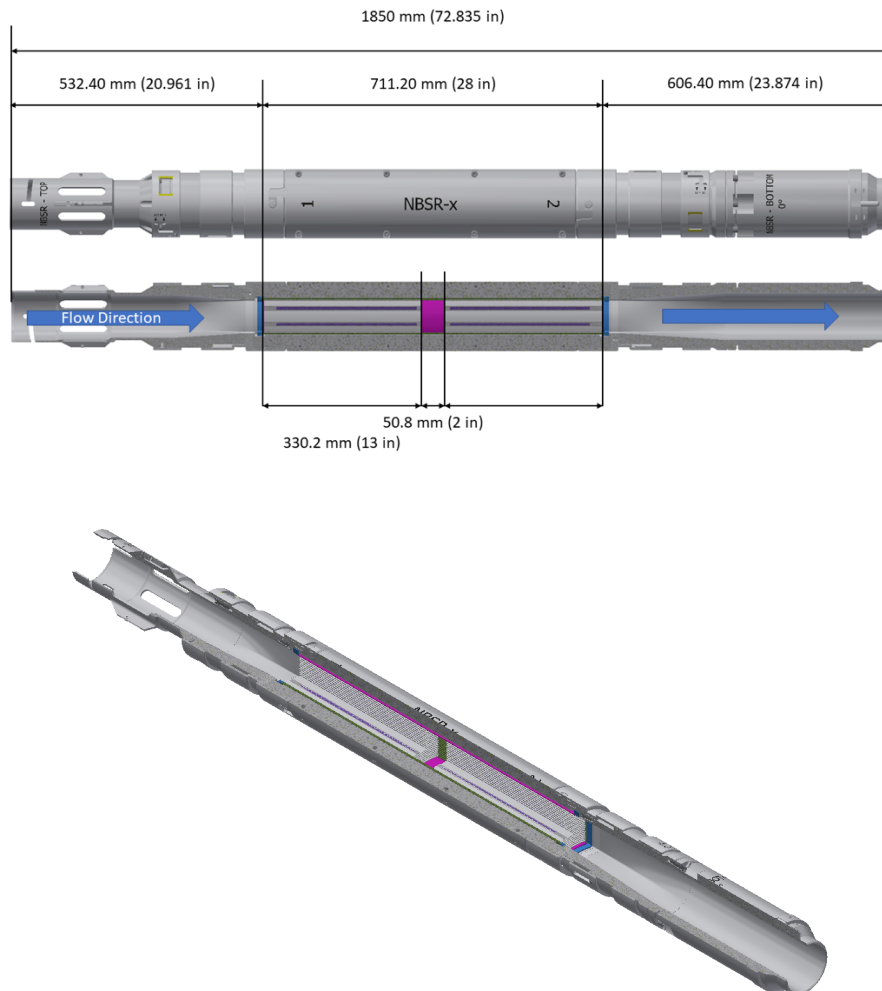


Figure 1. NBSR DDE basket and fuel assembly. Top: Axial cut showing key dimensions. Bottom: Axial cut showing the end fittings of the fuel assembly and gap.

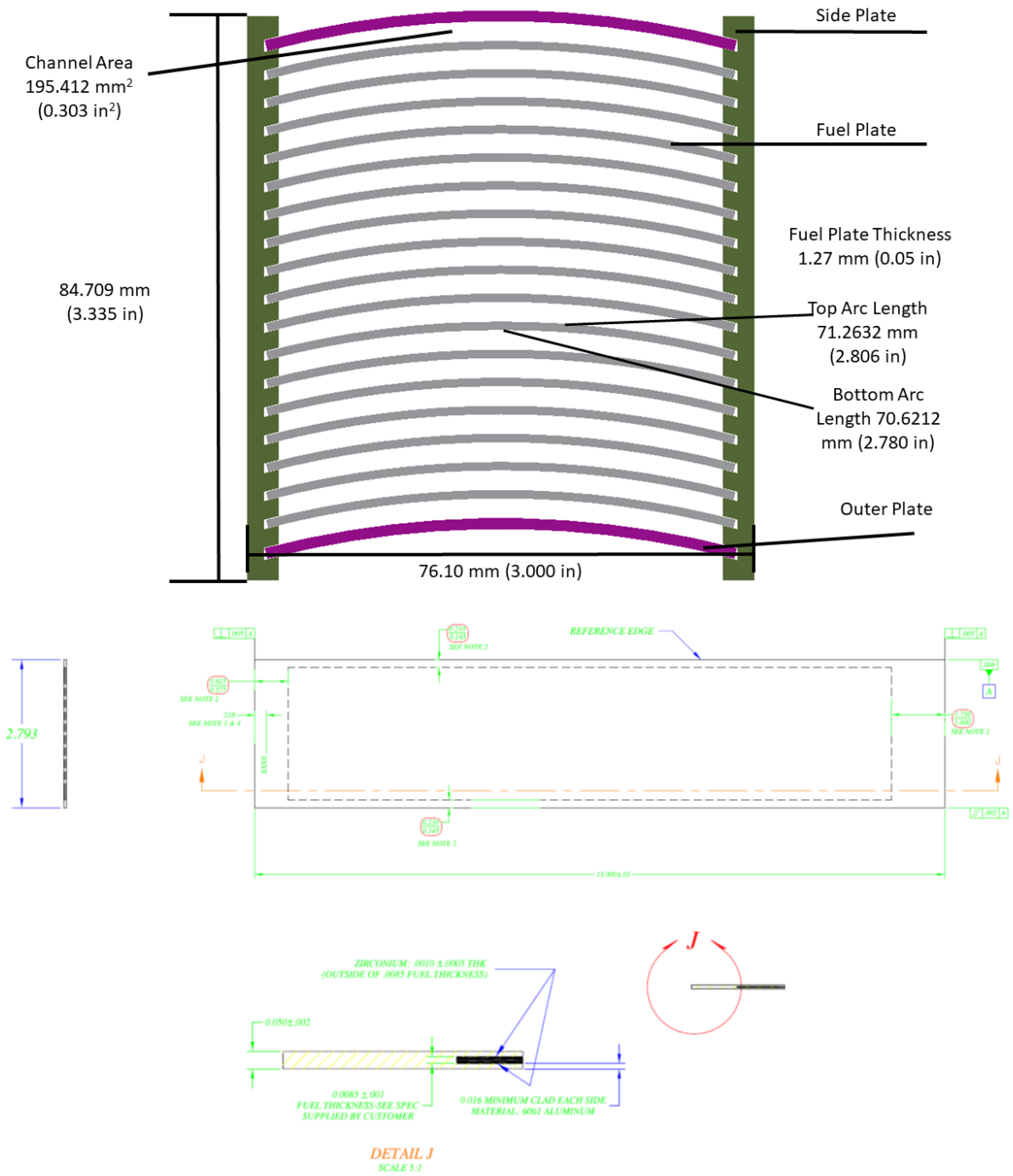


Figure 2. NBSR DDE fuel assembly plates.

## 2.2 BOUNDARY CONDITIONS

The power density distributions of NBSR DDE during the first and second irradiation campaigns have been provided from SCK CEN [Kalcheva, 2022] and are presented in Table 1. There are 10 irradiation cycles and the power density at each Beginning of Cycle (BOC) is provided. Three azimuthal discretizations were provided for the highest-power plate. This power was applied to all plates in the irradiation campaign.

This provides a bounding case for the calculation as this power is substantially higher than true distribution. The peak assembly power, corresponding to BOC06, is approximately 4 MW which was calculated from a simple integration of the power density over the volume. BOC corresponds to the beginning of cycle designation as that is how the data was provided. The reason the data starts at BOC-6 is because the irradiation campaign begins at BOC-1 with the MITR assembly and then at BOC-6 the NBSR assembly is also placed into the BR2 core. The axial power density is assumed uniform throughout analysis in this study and the azimuthal segments are equally sized.

Table 1. Power Density calculated and assumed in NBSR DDE fuel plates during the irradiation campaigns, the cycle time of each cycle was 31.5 days and the power during each irradiation campaign is assumed constant and equal to the Beginning of Cycle (BOC) power.

Irradiation Campaign	NBSR-Al-basket & Al-plug (12 Hf-rods)			
	Power Density (kW/cm <sup>3</sup> )			
	Azimuth	1 <sup>st</sup>	2 <sup>nd</sup>	3 <sup>rd</sup>
1 <sup>st</sup> standalone irradiation of NBSR-DDE in position H5	BOC 6, Power = 56 MW	12.21	11.36	12.86
	BOC 7, Power = 56 MW	10.64	10.05	11.19
	BOC 8, Power = 56 MW	9.48	9.04	10.07
2 <sup>nd</sup> simultaneous irradiation of NBSR-DDE in position H5 and NBSR-DDE in position H3	BOC 9, Power = 60 MW	9.04	8.76	9.81
	BOC 10, Power = 60 MW	8.09	7.73	8.62
	BOC 11, Power = 60 MW	6.93	6.67	7.26
	BOC 12, Power = 60 MW	6.08	5.89	6.54
	BOC 13, Power = 60 MW	5.18	5.17	5.47
	BOC 14, Power = 60 MW	4.83	4.84	5.14
	BOC 15, Power = 60 MW	4.10	3.87	4.38
EOL-NBSR-DDE	End of Cycle 15 = EOL for NBSR DDE			

The nominal average channel velocity of NBSR DDE [Bert, 2022] is 6.6 m/s. The nominal channel velocity is the flow velocity at cross-section of fuel region where the flow area is 3520.56 mm<sup>2</sup>. The frontal area of the inlet plenum duct in the CFD model is 6361.70 mm<sup>2</sup> according to the CAD model. The inlet velocity in the inlet plenum calculated by mass conservation to be 3.65 m/s. The pressure outlet boundary is specified by 0 Pa gauge pressure, while the operating pressure is set at 1.2 MPa. The inlet temperature into the domain is considered to be 308.15K, whereas free convection boundary conditions are imposed in the outlet section of this domain.

## 2.3 MATERIAL PROPERTIES

The built-in IAPWS-IF97 water properties were adopted to specify the density, viscosity, thermal conductivity, specific heat, and dynamic viscosity of working fluid for both the RELAP5-3D and CFD models. IAPWS-IF97 is a temperature- and pressure-dependent water property. The temperature dependent density, specific heat, and thermal-conductivity for the U-10Mo fuel [Rabin et al., 2017] and Aluminum 6061 cladding [Polkinghorne & Lacy, 1991] are provided in Table 2. For the mechanical

properties, Young's modulus and Poisson's ratio, no temperature or irradiation dependency is assumed. The values of these properties are taken as the one in the room-temperature, unirradiated configuration. No plastic deformations are expected and hence, only no plastic-deformation related properties are listed. Furthermore, the thermal diffusivity of the Zirconium liner between the fuel and the cladding is neglected.

Table 2. Thermophysical properties for fuel and cladding materials.

Material	Property	Equation	Temperature Validity Range
U-10Mo	Density [kg/m <sup>3</sup> ]	$\rho = -0.9215T[K] + 17409.0$	[293,623] K
	Specific Heat [J/(kg.K)]	$C_p = 0.0692T[K] + 113.61$	[293,623] K
	Thermal Conductivity [W/(m.K)]	$k = 0.0413T[K] + 0.1621$	[293,1073] K
	Young's Modulus [GPa]	88.4	-
	Poisson's Ratio [-]	0.41	-
Aluminum 6061	Density [kg/m <sup>3</sup> ]	$\rho = 2702.0$	[293,573] K
	Specific Heat [J/(kg.K)]	$C_p = 3.97 \times 10^{-5}T[K]^2 + 0.41T[K] + 773.0$	[298,805] K
	Thermal Conductivity [W/(m.K)]	$k = -1.73 \times 10^{-7}T[K]^3 + 2.66 \times 10^{-5}T[K]^2 + 0.16T[K] + 120.6$	[298,811] K
	Young's Modulus [GPa]	68.3	-
	Poisson's Ratio [-]	0.33	-

### 3. MODELS

The section summarizes the modeling approaches used for studying the thermal-hydraulics and mechanics fields. Thermal-hydraulics calculations are performed with RELAP5-3D (version 4.4.2) and STAR-CCM+ (version 17.02-R8). For validation of RELAP5-3D for this type of simulations we refer the reader to the references of this report [Miller & Shumway, 1992; Sloan et al., 1994; Weaver et al., 2002; Little, 2016; Maddock, 2017; RELAP5-3D, 2018; Narcisi et al., 2019; Collins, 2020; Martin & Williams,

2022]. Similarly, NQA-1 standard CFD modeling validation for this type of simulations for STAR-CCM+ can be bound in the provided references [Simcenter, 2020; Siemens, 2021; STAR-CCM+, 2021]. The mechanical calculations are performed with Abaqus 2021. ABAQUS quality assurance plan complies with the ISO 9001 and the ANSI/ASME NQA-1 quality assurance standards [Bryson & Dickson, 1993]. Details of the modeling approach implemented in each code are provided in the following subsections.

### 3.1 RELAP5-3D THERMAL-HYDRAULICS MODEL

The modeled flow geometry and configuration of the fuel plates in the NBSR fuel assembly is presented in Figure 3. The modeled geometry consists of an inlet pipe with a fitting to the fuel array, the internal subchannel space between the two sets of plates of the array, the gap in between the sets of plates, and the outlet fitting and pipe. The flow bypasses in the fuel assembly are not modeled in the RELAP5-3D model. The fuel plates are divided in three azimuthal sections. Each of the sections is not explicitly modeled in the RELAP5-3D model as V4.4.2 of the software does not include the possibility of capturing heat conduction in this transverse direction. Hence, the average power of the three azimuths is imposed in the RELAP5-3D model. Therefore, only transversely averaged profiles are captured in the RELAP5-3D model. This assumption resulted in a difference in the predictions between RELAP5-3D and CFD.

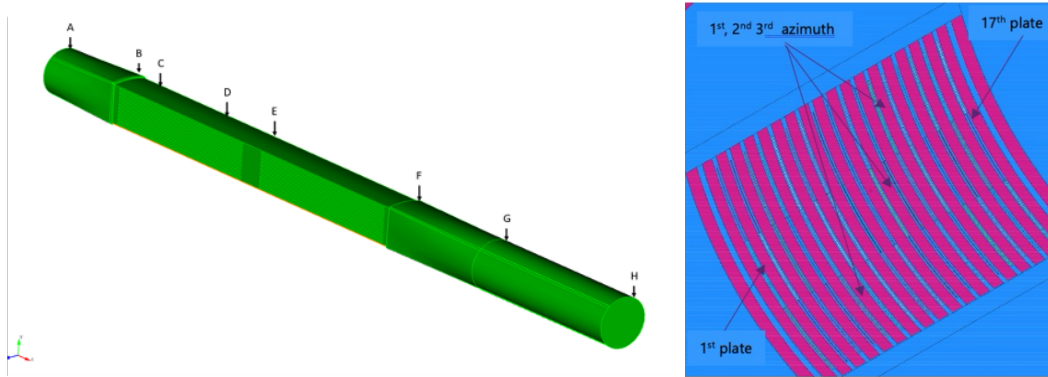


Figure 3. Left: modeled internal geometry for the fluid flow in the NBSR test section. Right: Structure of the fuel plates in the NBSR fuel assembly.

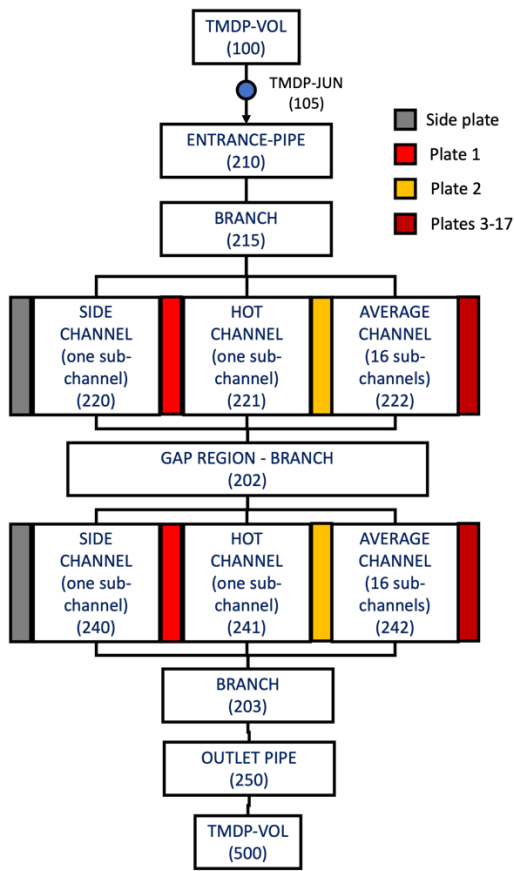


Figure 4. Nodal diagram for the RELAP5-3D NBSR model.

The nodal diagram of the RELAP5-3D model is depicted in Figure 4. The inlet section to the fuel assembly is modeled via a pipe component of varying area and hydraulic diameter. The entrance fitting to the fuel assembly is modeled via a branch component. A three-channel configuration is used to model the flow between plates for the top and bottom sets of plates. Channel 1 models the flow field between the side plate and fuel plate 1. Channel 2 models the subchannel between fuel plates 1 and 2. Finally, channel 3 models an averaged sub-channel composed by remnant 16 internal flow channels. Following static scaling principles, the flow rate and flow area in channel 3 are the sum of those channels composing channel-3 and the hydraulic diameter is the unweighted average of these ones. A branch component is used to model the gap between the two sets of plates. The flow geometry is closed with a branch component capturing the outlet fitting of the fuel assembly and the outlet pipe of varying hydraulic diameter.

One outer plate and the top and bottom plates 1 and 2 are explicitly modeled via a flow-perpendicular and axially discretized heat structure. In the flow-perpendicular direction, the thickness of the fuel plate is captured. In this direction the fuel plate is composed by the external aluminum cladding and the U10Mo. The volumetric power is imposed directly in the U10Mo fuel without considering direct heating of the Aluminum cladding. It is assumed that no nuclear power is being produced in the outer plate. Finally, plates 3 to 17 and the remaining outer plate are lumped together into one heat structure. Note that the temperature fields obtained within this average heat structure will be unrealistic. However, since the integral power and flow rates are modeled in the average plate and sub-channel, respectively, the surface temperature will be the average obtained for plates 3-17. Hence, the surface temperature predicted in this average plate can be used to study oxide growth rates. The average plate is complemented with a

symmetry boundary condition in the side of the plate not in thermal contact with the average cooling channel. Conjugated heat transfer is performed between fuel plates and the neighboring channels. For example, for plate 1 in the top set of plates, the left boundary condition will be provided by the temperature in channel 220 and the right one by the temperature in channel 221. The flow-perpendicular discretization of the plates is complemented with a cell left and right of the conjugated heat transfer boundaries. These cells are used to capture the oxide growth in the plate during irradiation. An initial oxide layer thickness of  $2\mu\text{m}$  is assumed for each plate side boundary. Simulations are performed sequentially from BOC-6 to BOC-15 and the oxide thickness is updated at each irradiation cycle ending to capture the historic effects of oxide-driven thermal insulation in the plates during irradiation.

Two final remarks close the RELAP5-3D model description. First, for all cases, mesh sensitivity studies have been carried out to ensure that the axial discretization for channels and pipes. This ensures that the discretization used is fine enough not to cause changes in the hydraulic pressure drop under successive refinements. Second, we note that by default, RELAP5-3D uses the bulk temperature to compute the Fanning friction factor for the pressure drop. However, due to the large heat fluxes in the plates, we observed that the temperature of the coolant next to the walls can significantly differ from those in the bulk of the channels. Therefore, modifications have been made RELAP5-3D to enforce the usage of the predicted next-to-wall temperatures when computing the Fanning friction factor. This led to significantly better comparisons against the CFD simulations.

## 3.2 STAR-CCM+ CFD MODEL

A steady-state, Reynolds-Averaged Navier-Stokes (RANS) equation-based conjugate heat transfer (CHT) analysis was conducted for the CFD analyses. A fluid domain of CFD model was solved by adopting a segregated flow solver with a second order convection scheme, a segregated fluid temperature solver, adding gravity, and with the realizable  $k - \omega$  (SST Menter) with all-  $y^+$  near wall model for the RANS closure. The solid domain was solved by adopting the segregated solid energy solver. The inlet and outlet of NBSR DDE were modeled with a velocity inlet boundary and the pressure outlet boundary, respectively. The power density is applied only at the fuel core. The oxide layer growth was modeled by the correlated Kim model [Kim et al., 2003; Kim et al., 2008]. The oxide layer was modeled as the thermal contact resistance between the cladding and coolant.

The simulation domain and mesh structure of NBSR-DDE is depicted in Figure 5. The computational mesh of NBSR DDE CFD model was generated by adopting the polyhedral mesh type with the prism boundary layers (4 layers) for the fluid domain and the polyhedral mesh with a thin mesher (3 layers) for the solid domain. Total number of cells in the computational mesh is 58.7 million. The base mesh sizes for fluid domain and solid domain are 0.5 mm and 2.5 mm, respectively. The maximum  $y^+$  that resulted from this simulation is  $\sim 10.5$

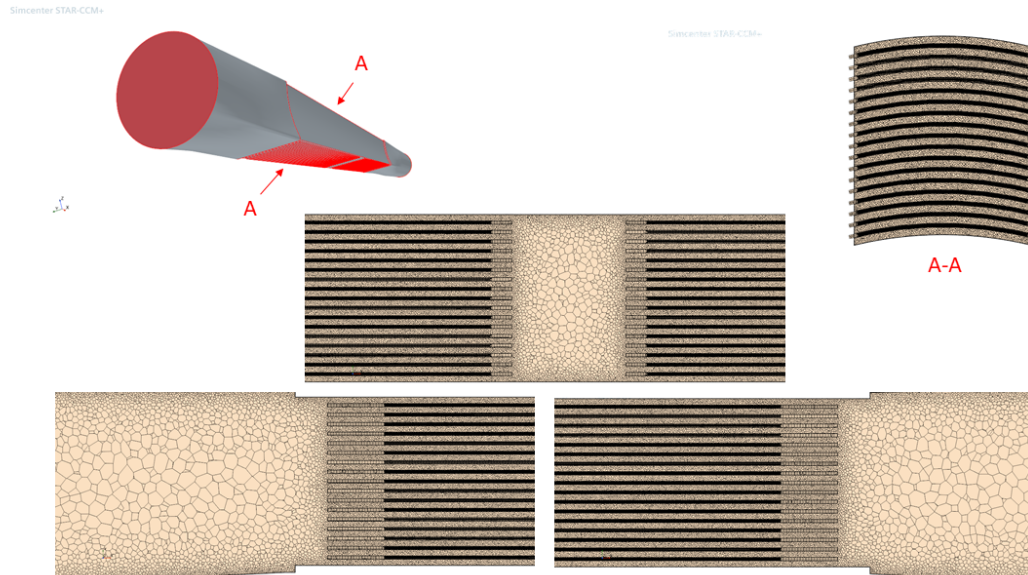


Figure 5. Domain geometry and mesh structure of NBSR DDE CFD model.

A mesh independence study was performed to ensure the CFD mesh was sufficiently converged to accurately capture key quantities of interest (QOI). The results of this study are shown in Figure 6. Pressure drop was used as a QOI and the convergence study was performed by approximately doubling the mesh count. As a result, the pressure drop changed by less than 2% across the whole domain giving confidence that the correct pressure drop is captured. If it is assumed the convergence change is a sort of uncertainty, then a three-sigma bound would be by 6% which is more than adequate for engineering uncertainties.

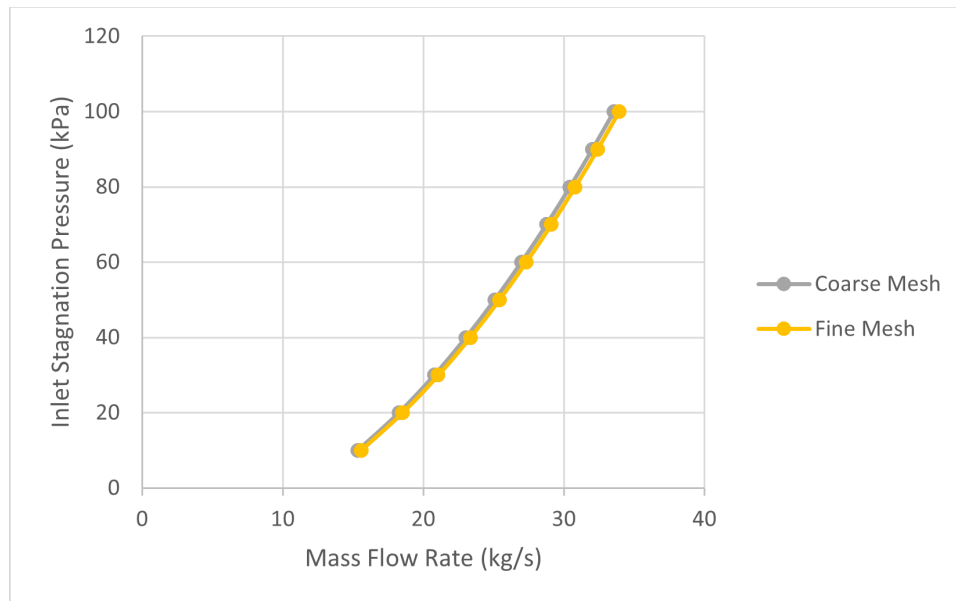


Figure 6. Grid Convergence behavior for various pressure drop across the DDE.

### 3.3 ABAQUS MECHANICAL MODEL

The pressures on two sides of one plate would not be equal due to non-uniform flow distributions to the flow channels as well as the heating effect. Only deformation of the plate due to the pressure difference is evaluated in the ABAQUS calculation. Independent linear elastic deformation studies are performed for each plate. Figure 7 shows the loads for the fuel assembly and boundary conditions per plate. Pressures are imposed perpendicular to each plate, while a non-displacement boundary condition is imposed on the long edges of the plates. The pressure distributions on the cladding surfaces that are exported from the CFD calculation using a STAR-CCM+ table, and then imported to ABAQUS using a custom-developed Python script. The gravitational force is also considered in the Abaqus model.

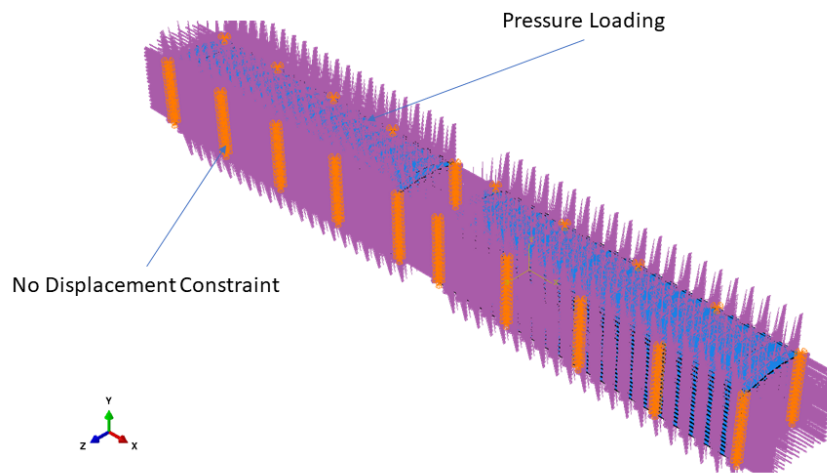


Figure 7. Pressure load and constraint boundary condition of ABAQUS model.

## 4. STUDY RESULTS

The present section summarizes key results of the study. Previous validation work of comparing the RELAP5-3D and CFD simulations to validate the modeling hypotheses were done for the MITR DDE [Tano & Yoon, 2022]. The reader is referred to this report for details about this cross-validation approach. The non-isothermal pressure-drop, velocity profiles, temperature, and heat transfer coefficient distributions are studied for all BOC configurations; from BOC-6 to BOC-15. Next, the oxide growth over the plates is studied for all BOC configurations. Finally, the deformations and stress distributions over the plates are analyzed.

### 4.1 THERMAL-HYDRAULICS FIELDS FOR NON-ISOTHERMAL CONDITIONS

The total pressure drops and pressure profiles predicted with the RELAP5-3D and CFD models, respectively, is compared for all BOC configurations in Figure 8. The pressure profile is qualitatively similar to between both simulations and hence, only the CFD profiles are presented. Pressure drop is approximately negligible in the inlet pipe but much larger in the DDE channels. As approximately

singular pressure drop (rise) is observed at the inlet (outlet) fitting of the fuel assembly due to the sudden flow acceleration into (deceleration out of) the fuel assembly. A similar effect occurs at the channel gap, where pressure suddenly rises and reduces as the flows decelerates into the gap and accelerates into the bottom channels, respectively. It is observed that the total pressure drop change  $\sim 15$  kPa due to the difference in heating across the analyzed configurations according to the RELAP5-3D model, whereas a smaller change of  $\sim 3$  kPa is predicted by the CFD models. The reason for this difference is that an empirical is used RELAP5-3D to estimate the near-wall viscosity when computing the pressure drop, which leads to an over estimation of the temperature effects on the pressure profiles. Hence, the CFD results are preponderantly trusted in this case. The largest difference in pressure drop is predicted between BOC-6 (hottest) and BOC-15 (coldest) configurations. The hottest configurations present a reduction in pressure drop, due to the reduction in the flow viscosity. Nonetheless, the changes in pressure drop due to heating are only about 10% of the total pressure drop over the assembly and, hence, a second order effect in the pressure drop.

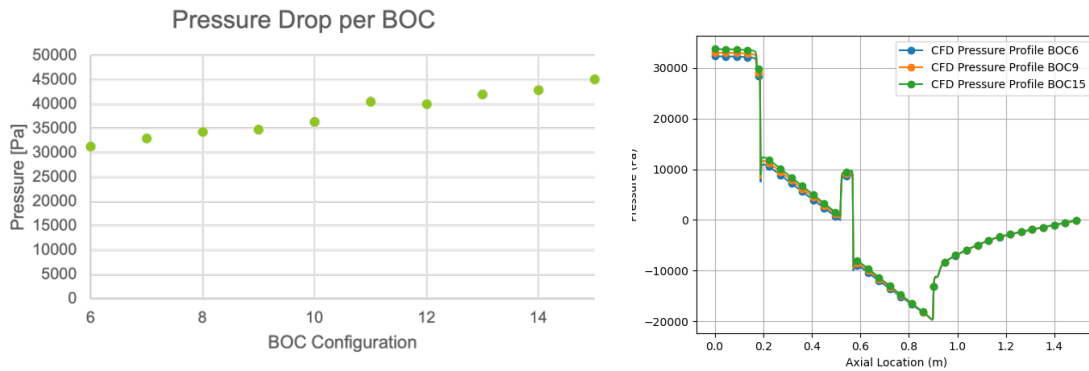


Figure 8. Left: total pressure drops predicted for all BOC configurations with the RELAP5-3D model. Right: pressure profiles predicted with the CFD model for all BOC configurations.

It is observed that the pressure drop increase from BOC-6 to BOC-15 due to the reduction in heating power and due to the shrinkage of the channels because of oxide growth; this latter effect is only captured in the RELAP5-3D model. The effect of the oxide growth on the pressure drop has been estimated to be  $\sim 0.2$  kPa. Hence, this effect is, at most, a third order effect in the pressure profiles. Therefore, these effects could be disregarded from the pressure drop when performing mechanical pressure drop studies for the NBSR DDE.

CFD-calculated cross-sectional velocity distributions at the entrance, middle, and exit of the fuel region for the example BOC-6 are presented in Figure 9. By comparing the entrance and exit of the fuel region one can observe a non-negligible axial flow development through the channel. Moreover, the curvature of the plates tends to increase flow at the center of the channels due to centrifugal acceleration. Therefore, higher velocities are obtained at the center of the channels. As the fluid is heated the density of water will decrease, increasing the velocity of the flow in the channels. As the NBSR DDE power density decreases through the irradiation campaign the flow velocity should decrease as well. No bypass flow was modeled in the NBSR DDE and so the full specified flow rate was used for cooling the plates.

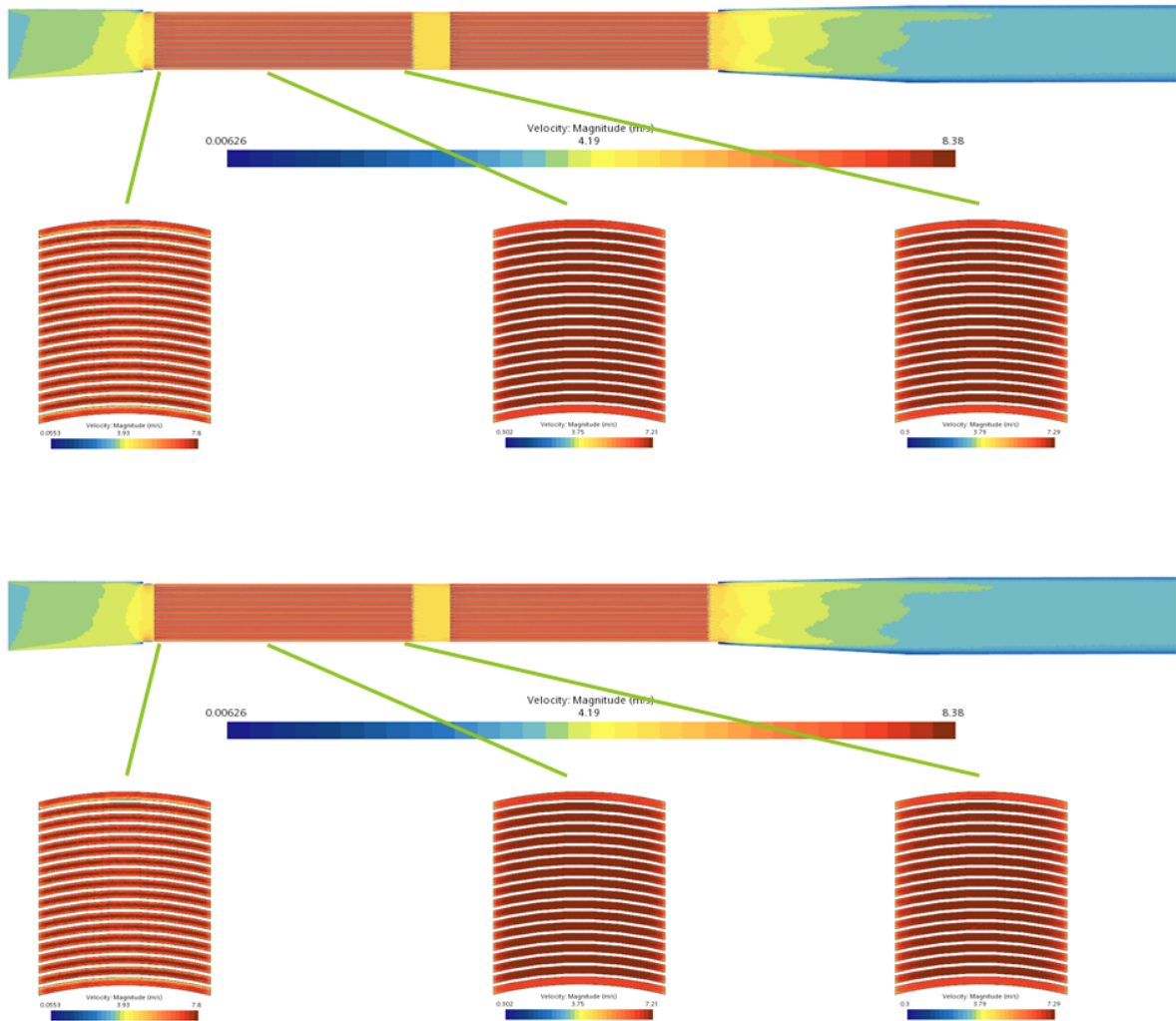


Figure 9. CFD-calculated cross-sectional velocity distributions at various locations. Top: top set of plates. Bottom: bottom set of plates.

The maximum and average velocity and the surface average velocity as a function of axial position are presented in Figure 10. The analysis of the maximum velocities shows that the density changes through the channel as the fluid is heated does not significantly affect the channel flow distribution. The analysis of the average velocity shows the velocities are relatively stable through the channels and throughout the cycles even with a change in assembly power. This supports the differences in pressure profiles being a function of the bulk and wall viscosity since the velocity is not sensitive to the power.

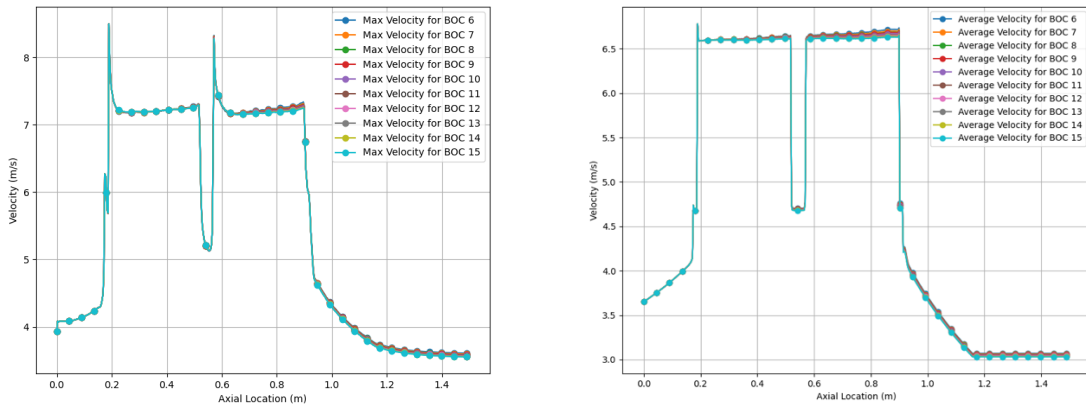
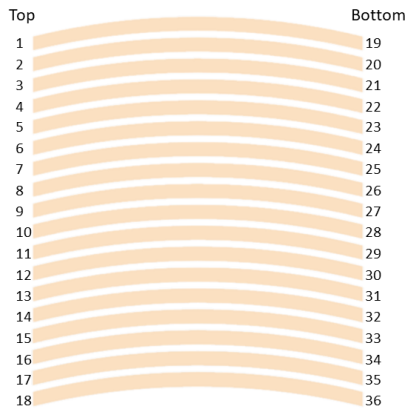


Figure 10. Left: Maximum Channel Velocity as a function of Axial Position. Right: Average Channel Velocity as a function of Axial Position.

Other useful information is the fuel subchannel mass flow rate for each channel. This shows the deviation from a standard assumption that the flow distributes evenly between the channels. Figure 11 shows the distribution of flow within the channels in the upper and lower set of plates. The hypothesis of evenly distributed flow is approximately appropriate.



Channel Number	Top Channel (kg/s)	Channel Number	Bottom Channel (kg/s)
1	1. 207646	19	1. 296876
2	1. 289605	20	1. 289825
3	1. 291758	21	1. 288797
4	1. 295408	22	1. 286956
5	1. 29668	23	1. 284963

6	1. 299288	24	1. 283561
7	1. 299843	25	1. 283671
8	1. 298778	26	1. 280143
9	1. 303925	27	1. 285579
10	1. 304023	28	1. 290053
11	1. 300262	29	1. 282679
12	1. 299844	30	1. 285545
13	1. 298757	31	1. 282477
14	1. 298848	32	1. 285075
15	1. 299191	33	1. 289179
16	1. 301517	34	1. 294138
17	1. 303105	35	1. 2941
18	1. 188529	36	1. 281897

Figure 11. Top: Flow channels numbering. Bottom: mass flow rate per subchannel during BOC-6.

The transversal-averaged coolant temperature profiles for all BOC configurations are presented in Figure 12. Since these results respond solely to enthalpic balance, only the RELAP5-3D results are computed. CFD results are equivalent within a tolerance of 0.1%. The temperature rise decreases from BOC-6 to BOC-15 as the heating power decreases. The thermal protective effects of the oxide growth layer do not play a significant role in the average temperature of the coolant. This is expected since the coolant average temperature rise should be determined by the enthalpy balance between the heat added into the flow and the temperature rise. The maximum temperature is of ~40K for BOC-6.

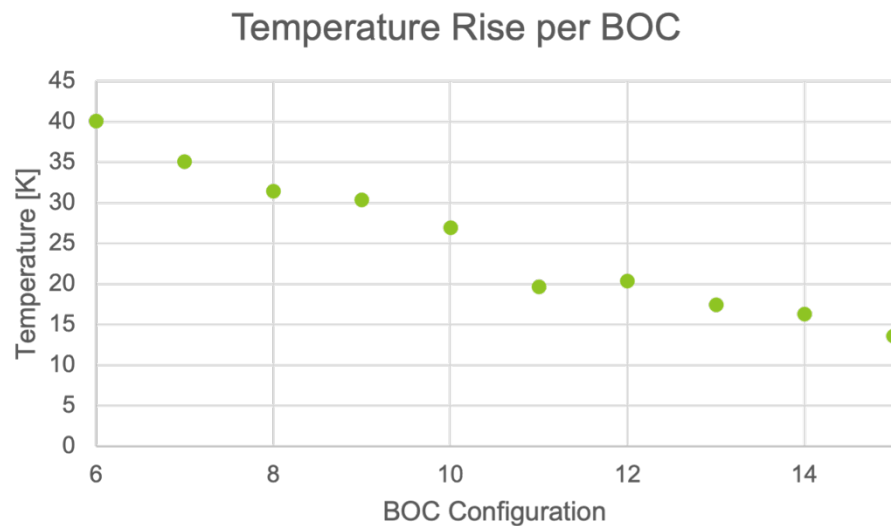


Figure 12. Comparison of the total temperature rise over the full section for all BOC configurations for the RELAP5-3D models; CFD results are equivalent within 0.1% of tolerance.

CFD predicted peak fuel and peak cladding temperatures are presented in Figure 13. The bands in these figures represent the range of variations across fuel plates. The trend is very clear and follows the decrease in assembly power very closely. The impact of oxide thickness on the plates is small as the thickness of the oxide is not large and the resultant thermal resistance is small as well. Since all the plates had the same power distribution, there was a heavy dependence on the local bulk fluid temperature in the temperature distributions. This is indicated by the bottom plates, nearest the assembly exit, had the highest temperatures while the top plates had lower temperatures. As we will see later this trend is also seen in the oxide growth distribution.

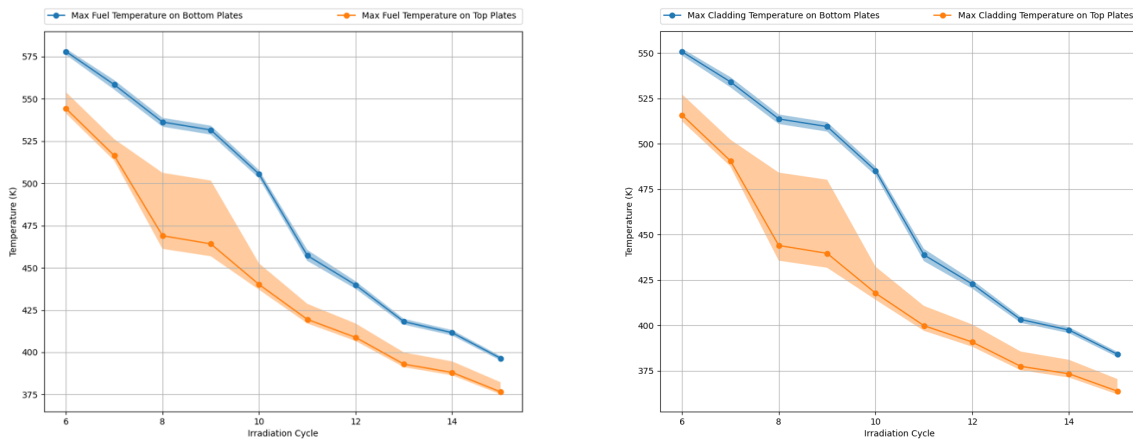


Figure 13. Left: Maximum fuel temperature as a function of the plate in the assembly for each irradiation Cycle. Right: Maximum temps predicted in the Fuel and Cladding by the CFD simulation.

The plate averaged heat transfer coefficient distributions is depicted Figure 14. The bands in this figure represent the range of variation across plates. In Star-CCM+ the heat transfer coefficient is predicted from a reference temperature that is set by the user rather than the local bulk temperature. This reference temperature was set as the inlet temperature (308K). If the reference temperature would be the local bulk velocity, it would be expected to have a much more uniform distribution as the channel geometry, flow, and temperatures do not deviate from each other. By referencing from the inlet temperature, there is a bias introduced by the gradual heat-up of the fluid.

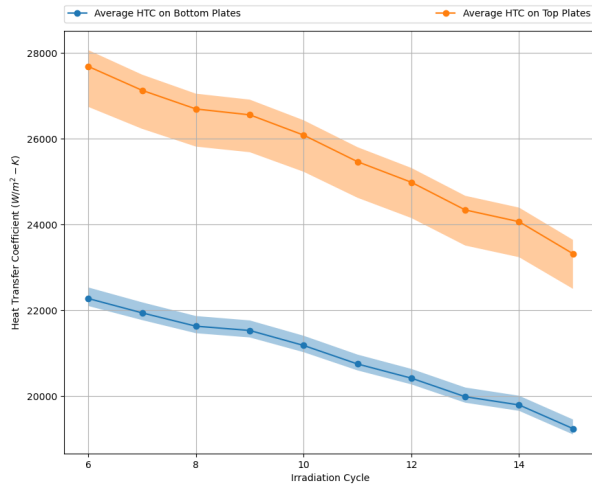


Figure 14. Plate averaged heat transfer coefficients as a function of irradiation cycle.

## 4.2 OXIDE GROWTH STUDIES

The CFD model uses local thermal conditions to determine oxide layer growth rates and as a result is expected to provide more accurate estimations of the oxide layer thickness in general. The oxide layer growth is highly non-linear and as a result small deviations in the temperature and fluxes could result in large differences, so averaged or homogenized models could under predict growth. Figure 15 shows the average and maximum oxide thickness predictions on each plate throughout the irradiation campaign. The oxide thickness that CFD predicts is much thicker than what RELAP5-3D predicts from both an average and maximum perspective. The lower plates show a significantly thicker layer as a result of being subject to hotter bulk fluid temps. The behavior of the growth is as expected. The earlier cycles have much higher power generation and result in the largest rate of growth for the oxide layer. As the power decreases through the campaign the thickness asymptotically approaches a steady value and the oxide layer stops growing. The CFD models used Kim's correlation for oxide growth.

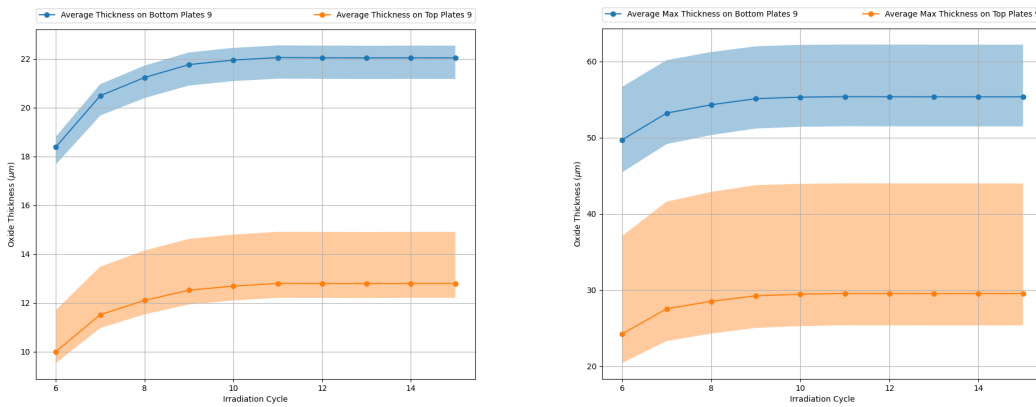


Figure 15. Left: Average Oxide Thickness predicted on each plate throughout the irradiation campaign. Right: Maximum oxide Thickness predicted on each plate throughout the irradiation campaign.

### 4.3 STRUCTURAL ANALYSES

The curved plates of the NBSR geometry give additional geometric rigidity to protect against buckling. Figure 16 show the stress and displacements for the example BOC-6 configuration. The maximum displacement as a result of this heating profile is 2.085  $\mu\text{m}$  and the maximum stress in all plates in 1.662 MPa. The maximum displacements and stresses for BOC-6, BOC-9, and BOC-15 are presented in Table 3. The largest stresses are obtained for BOC-15 as the larger pressure differential between plates is obtained for this configuration. In general small stresses are observed, which are well below the transversal yield stress for the plate (274 MPa).

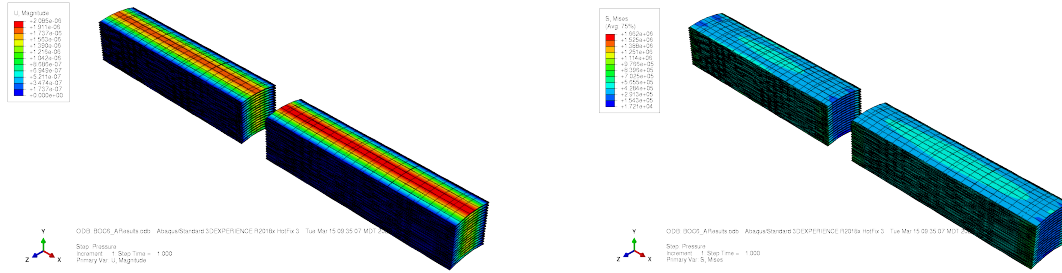


Figure 16. Left: ABAQUS calculation results for BOC6 (left: plate displacement, right: Von Mises stress).

Table 3. Maximum displacements and stresses for selected BOC configurations.

Configuration	Maximum Displacement ( $\mu\text{m}$ )	Maximum Stress (MPa)
BOC-6	2.085	1.662
BOC-9	2.057	1.682
BOC-15	2.055	1.687

### 5. CONCLUSIONS

In this report, the thermal-hydraulic calculations using system thermal-hydraulic code, RELAP5-3D, and computational fluid dynamics software, STAR-CCM+, and the mechanical analysis using FEA code, Abaqus were conducted to support the analysis of NBSR DDE. Key findings of this report are as follows:

- RELAP5-3D and CFD predictions for the pressure drop over the whole test section (inlet pipe, fuel assembly, and outlet pipe) agreed well qualitatively. However, RELAP5-3D presented a larger dispersion in the pressure drop profiles with heating than CFD and a larger pressure drop over the inlet pipe due to the approximated development length model. This indicates that both RELAP5-3D and CFD could be used for performing studies of pressure drops for different flow rates. However, RELAP5-3D friction models must be adjusted to explicitly use near-wall temperatures for computing the skin friction coefficients as the code uses bulk temperature by default leading to over-estimated pressure drops.
- Transverse-averaged temperature over the fuel plates agree very well between RELAP5-3D and CFD analyses. The maximum averaged temperature rise for the coolant in the fuel plates was  $\sim 40$  K for BOC-6, whereas the minimum one was  $\sim 14$  K for BOC-15. We recommend

performing the computations of the maximum cladding and fuel foil temperatures using CFD as RELAP5-3D results can be under-conservative.

- The CFD with correlated Kim Model predicted that the maximum thickness of the oxide layer would be  $\sim 62 \mu\text{m}$  at the end of BOC-15. CFD's prediction was much greater than RELAP5-3D prediction. The lumped modeling approach of RELAP5-3D would underestimate the maximum oxide layer thickness. Further investigation and validation for the oxide layer growth models are needed.
- Abaqus analysis results showed that hydrodynamic pressure-induced plate deformation and structural stress are negligible when regarding the pressure drop and flow distribution over the test section.

## 6. REFERENCE

Bryson, J. W., & Dickson, T. L. (1993). *Stress-intensity-factor influence coefficients for axial and circumferential flaws in reactor pressure vessels* (No. CONF-930702--4). Oak Ridge National Lab.

A. Collins, "VTR modeling and simulation using INL RELAP5 system code, ECAR-4788, 2020.

B. Rabin, M. Meyer, J. Cole, I. Glagolenko, G. Hofman, W. Jones, J. Jue, D. Keiser Jr, Y. Kim, C. Miller, et al., "Preliminary report on u-mo monolithic fuel for research reactors," Idaho National Laboratory INL/EXT-17-40975, 2017.

B. Rossaert, "Bridges-mustang-r critical velocity analysis for NBSR and nsbr, calculation note-nc4986/n0brid-des/02/br," Restricted Contract Report SCK CEN/46944057 (R-8944), 2022.

C. Miller and R. Shumway, "Relap5/mod3 code quality assurance plan for ornl ans narrow channel flow and heat transfer correlations," EG and G Idaho, Inc., Idaho Falls, ID (United States), Tech. Rep., 1992.

C. Xing, "Thermal Performance of the AFIP-7 Fuel Assembly in the ATR Center Flux Trap," ECAR-4741, 2019.

J. C. Griess, H. C. Savage, and J. L. English, "Effect of heat flux on the corrosion of aluminum by water. part iv. tests relative to the advanced test reactor and correlation with previous results," ORNL-3541, 1964. DOI:10.2172/4077613. [Online]. Available: <https://www.osti.gov/biblio/4077613>.

R. E. Pawel, "On the kinetics of the aluminum-water reaction during exposure in high-heat flux test loops: 1, a computer program for oxidation calculations," ORNL/TM-10602, 1988. DOI:10.2172/5524442. [Online]. Available: <https://www.osti.gov/biblio/5524442>.

R. Little, "Results of Physics Calculations in Support of RELAP5 analysis of the enhanced LEU fuel (ELF) MK 1A," ECAR-2469, 2016.

R. Martin and J. Williams, "Safety software evidence ranking for determining analytical readiness with a case study utilizing relap5-3d," in The 19th International Topical Meeting on Nuclear Reactor Thermal Hydraulics (NURETH-19), Mar. 2022.

RELAP5-3D Code Development Team, "Relap5-3d code manual. volume 4, models and correlations," Idaho National Laboratory, Tech. Rep., 2018.

Release notes for relap5-3d version 4.4.2.2021. [Online]. Available: <https://relap53d.inl.gov/Shared%5C%20Documents/Release%5C%20Notes/Release%5C%20Notes%5C%20for%5C%20RELAP5%5C%204.4.2.pdf>.

S. J. Pawel, D. K. Felde, and R. Pauer, "Influence of coolant pH on corrosion of 6061 aluminum under reactor heat transfer conditions," ORNL/TM-13083, 1995. DOI:10.2172/205846. [Online]. Available: <https://digital.library.unt.edu/ark:/67531/metadc671895>.

S. Polkinghorne and J. Lacy, "Thermophysical and Mechanical Properties of ATR Core Materials," EG&G Idaho Inc., Internal Technical Report, 1991.

S. Sloan, R. Schultz, and G. Wilson, "Relap5/mod3 code manual," EG and G Idaho, Inc., Idaho Falls, ID (United States). Idaho National ..., Tech. Rep., 1994

S. Kalcheva, "Feasibility study for dde-NBSR and nsbr irradiation in br2 november 2021 - ed01," SCKCEN, Document BR2-RCE-RFA, Table XIX (NBSR DDE) and XX (NBSR DDE), 2021.

Siemens Digital Industries Software, STAR-CCM+ User Guide 2022.1.1, 2021.

Simcenter star-ccm+ verification suite, 2020.

STAR-CCM+ Software Completes ASME NQA-1 Compliance Press Release, 2021. [Online]. Available: <https://www.plm.automation.siemens.com/global/en/our-story/newsroom/siemens-press-release/43868>.

T. L. Maddock, "Results of Physics Calculations in Support of RELAP5 analysis of the enhanced LEU fuel (ELF) design," ECAR-2230, 2017.

Thermal Performance of the FUTURE-HFIR fuel plates in the BR2 reactor, ECAR-5107, 2019.

V. Narcisi, P. Lorusso, F. Giannetti, A. Alfonsi, and G. Caruso, "Uncertainty quantification method for relap5-3d© using raven and application on nacie experiments," *Annals of Nuclear Energy*, vol. 127, pp. 419–432, 2019.

W. L. Weaver, E. Tomlinson, and D. Aumiller, "A generic semi-implicit coupling methodology for use in relap5-3d©," *Nuclear Engineering and Design*, vol. 211, no. 1, pp. 13–26, 2002.

Y. S. Kim, G. Hofman, A. Robinson, J. Snelgrove, and N. Hanan, "Oxidation of aluminum alloy cladding for research and test reactor fuel," *Journal of Nuclear Materials*, vol. 378, no. 2, pp. 220–228, 2008, ISSN: 0022-3115. DOI: <https://doi.org/10.1016/j.jnucmat.2008.06.032>. [Online]. Available: <https://www.sciencedirect.com/science/article/pii/S0022311508003590>.

Y. S. Kim, G. L. Hofman, N. A. Hanan, and J. L. Snelgrove, "Prediction model for oxide thickness on aluminum alloy cladding during irradiation," in *2003 International Meeting on Reduced Enrichment for Research and Test Reactors (RERTR)*, Chicago, IL, Oct. 2003.